Materials Science & Engineering A 761 (2019) 137967

Contents lists available at ScienceDirect

Materials Science & Engineering A

journal homepage: www.elsevier.com/locate/msea

# Fracture of laser powder bed fusion additively manufactured Ti–6Al–4V under multiaxial loading: Calibration and comparison of fracture models

Alexander E. Wilson-Heid[a], Allison M. Beese[a,b,*]

[a] Department of Materials Science and Engineering, Pennsylvania State University, University Park, PA, 16802, United States
[b] Department of Mechanical Engineering, Pennsylvania State University, University Park, PA, 16802, United States

ARTICLE INFO

*Keywords:*
Multiaxial fracture
Additive manufacturing
Laser powder bed fusion
Ti–6Al–4V
Fracture prediction

ABSTRACT

The fracture behavior of laser powder bed fusion (L-PBF) additively manufactured Ti–6Al–4V alloy manufactured in two orientations was investigated using a combined experimental and computational simulation approach. To quantify the effect of stress state on fracture of L-PBF Ti–6Al–4V, mechanical tests subjecting the material to seven distinct stress states were performed. For each test performed, computational simulations were used to determine the evolution of plastic strain and the stress state parameters stress triaxiality and Lode angle parameter up to fracture. Six existing fracture criteria were calibrated, and their ability to capture and/or predict the fracture behavior over a wide range of stress states was evaluated. It was determined that fracture models that explicitly take into account the effects of both the stress triaxiality and Lode angle parameter more accurately captured the multiaxial failure behavior of L-PBF Ti–6Al–4V compared to models that consider no stress state-dependence or only a dependence on stress triaxiality. Additionally, samples loaded in the vertical build direction had a higher ductility than corresponding samples loaded perpendicular to the vertical build direction. The stress state-dependent fracture behavior of L-PBF Ti–6Al–4V quantified in this study highlights the importance of experimentally measuring the fracture behavior of this material under a range of stress states that could be accessed during service, and defining appropriate models to prevent failure in components.

## 1. Introduction

Additive manufacturing (AM) can be used to produce geometrically complex parts in a layer-by-layer fashion [1]. In particular, laser powder bed fusion (L-PBF) can be used to manufacture solid metallic components starting with raw powder metal feedstock and a laser heat source. In L-PBF, a laser is used to selectively melt a 2D pattern in a thin layer of powder, typically between 30 and 100 μm tall, fusing the current layer to either the baseplate or a previously solidified layer below. Layers are continuously added by lowering the baseplate by the desired layer height, spreading a new layer of powder, melting the next 2D layer pattern into the new powder layer using the laser heat source, and repeating the process until the 3D component is fabricated. The L-PBF process imparts rapid melting, solidification, and repeated heating and cooling cycles to the material with the addition of layers, resulting in unique process-structure-property relationships in parts made by L-PBF.

Prior to AM becoming a viable alternative to traditional manufacturing techniques for structural components in industries such as aerospace, transportation, biomedical, etc. [2–4], a complete understanding of the mechanical behavior up to and including fracture must be in place. Using AM to design and fabricate complex geometries for light-weighting in these industries can result in complex stress states in these components during service, and in particular, spatially varying stress states. Therefore, it is important to characterize the multiaxial mechanical properties of additively manufactured materials in order to predict component performance and design against failure.

Ti–6Al–4V, the most commonly used titanium alloy globally, is an α/β phase alloy that is used in applications where high strength, stiffness, and corrosion resistance are desired [5]. The AM community has performed significant research aimed at understanding the behavior of additively manufactured Ti–6Al–4V in areas such as: strength, ductility, anisotropy, fatigue, and corrosion resistance [6–10]. However, there is limited published data on the elasto-plastic and fracture behavior of additively manufactured Ti–6Al–4V over a broad range of stress states [11,12], as most research has focused only on mechanical properties under uniaxial tension (UT).

In previous work by the authors, a stress state-dependent, anisotropic plasticity model was calibrated and validated for L-PBF Ti–6Al–4V through experiments under five different stress states for

* Corresponding author. Department of Materials Science and Engineering, Pennsylvania State University, University Park, PA, 16802, United States.
*E-mail address:* beese@matse.psu.edu (A.M. Beese).

https://doi.org/10.1016/j.msea.2019.05.097
Received 29 April 2019; Received in revised form 24 May 2019; Accepted 25 May 2019
Available online 02 June 2019

samples extracted in two build orientations [13]. The yield and subsequent flow behavior of the L-PBF Ti–6Al–4V studied was found to be stress state-dependent. Additionally, in all stress states, samples loaded parallel to the vertical build direction were stronger than samples loaded perpendicular to the vertical build direction; however, the anisotropy was minor. The calibrated plasticity model, which is also used in the present study, consisted of a Hill 1948 anisotropic yield criterion [14], associated flow rule, and isotropic hardening law.

The fracture community has proposed many models to describe ductile metal failure, including phenomenological and empirical models based on strain, stress, or mixed stress/strain criteria. The present study focuses on the effect of stress state on fracture of additively manufactured Ti–6Al–4V. As background, two non-dimensional parameters may be used to fully describe a material's stress state: stress triaxiality and Lode angle parameter. Stress triaxiality, η, is a function of the first invariant of the Cauchy stress tensor, $\boldsymbol{\sigma}$, and the second invariant of the deviatoric stress tensor, $\boldsymbol{s}$, and is given as:

$$\eta = \frac{\sigma_m}{\bar{\sigma}} \tag{1}$$

where $\sigma_m = \frac{1}{3}I_1$ is the mean stress, $I_1 = \sigma_{kk}$ is the first invariant of the Cauchy stress tensor, $\bar{\sigma} = \sqrt{3J_2}$ is the von Mises equivalent stress, and $J_2 = \frac{1}{2}s_{ij}s_{ij}$ is the second invariant of the deviatoric stress tensor. The normalized Lode angle parameter, $\bar{\theta}$, is a function of the third invariant of the deviatoric stress tensor, $J_3 = det(s_{ij})$, and is defined as:

$$\bar{\theta} = 1 - \frac{2}{\pi} arccos\left[\frac{27}{2}\frac{J_3}{\bar{\sigma}^3}\right] \tag{2}$$

Under plane stress conditions ($\sigma_3 = 0$), the relationship between the Lode angle parameter and stress triaxiality is given as:

$$\sin\left(\frac{\pi}{2}\bar{\theta}\right) = -\frac{27}{2}\eta\left(\eta^2 - \frac{1}{3}\right) \tag{3}$$

The fact that the fracture behavior of ductile metals depends on stress state has been well established, resulting in models that define fracture as a function of stress state. Some models are physically informed and consider void nucleation, growth, and coalescence in high stress triaxiality fracture [15–18], or shear band formation in shear dominated fracture [19]. Other models are empirical and strictly based on experimental studies that assess the role of stress triaxiality on the fracture behavior [20–22]; this includes the well-known Johnson-Cook model, which captures the decreasing strain to failure with increasing stress triaxiality [20]. More recent models have pointed out the need for considering the impact of the third invariant, or the incorporation of Lode angle dependence, to accurately capture fracture behavior of ductile metals [23,24].

Wierzbicki et al. compared the ability of seven different fracture models to capture the multiaxial ductile failure behavior of a conventionally processed metal (2024-T351 aluminum alloy) in the equivalent plastic strain to failure versus stress triaxiality space, and found that the maximum shear stress criterion [25] worked well to predict failure over a wide range of stress triaxialities while only requiring one test for calibration [26]. However, they found that incorporating the effect of stress triaxiality and a parameter dependent on the third invariant of the stress deviator, for example in the Xue-Wierzbicki model, more accurately captured the failure behavior of the aluminum alloy studied [26].

Using both stress state parameters ($\eta$ and $\bar{\theta}$), Bai et al. proposed an asymmetric fracture model in the $[\bar{\varepsilon}_f, \eta, \bar{\theta}]$ 3D space, referred to as the modified Mohr-Coulomb (MMC) fracture model [24]. The phenomenological model, which takes into account the contribution of the Lode angle parameter on the failure strain of a material, has been successfully used to capture the fracture behavior of many ductile metals [27–29]. In addition to the MMC model, the Hosford-Coulomb (HC) fracture initiation model developed by Mohr and Marcadet [30] describes the equivalent strain to failure as function of both stress triaxiality and Lode angle parameter. A primary difference between the MMC and the HC model is that the dependence on shear stress in the HC model is incorporated through the Hosford equivalent stress, which takes into account the second principal stress [31], while the Mohr-Coulomb (MC) model, on which the MMC model is based, uses the Tresca equivalent stress, or maximum shear stress, disregarding the intermediate principal stress [32]. The HC model has been used to effectively characterize the failure behavior of high strength steels and an aluminum alloy [30,33].

There has not yet been a study published on the multiaxial fracture behavior of L-PBF Ti–6Al–4V, nor a fracture model proposed for L-PBF Ti–6Al–4V. The fracture behavior of both conventionally processed and directed energy deposited (DED) additively manufactured Ti–6Al–4V have been studied and reported in the literature. Giglio et al., calibrated a two-branch empirical curve fit fracture criteria in $[\bar{\varepsilon}_f, \eta]$ space for conventional Ti–6Al–4V, similar to the method used by Bao and Wierzbicki [21]. Hammer et al., calibrated a 3D fracture locus, for rolled Ti–6Al–4V plate, in the $[\bar{\varepsilon}_f, \eta, \bar{\theta}]$ space and found that stress triaxiality by itself does not capture the failure behavior of this material [34,35]. For wire-DED Ti–6Al–4V, Tancogne-Dejean et al. developed a probabilistic fracture model based on the HC model described above [11]. The probabilistic version of the HC model incorporates an additional model parameter, compared to the original HC model, to take into account the scatter in the experimental results for the bulk additively manufactured material. For the same wire-DED Ti–6Al–4V material, Gorji et al. experimentally measured the hardening and fracture behavior of the large individual prior-β grains (18 mm tall and several mm wide) in this material, and developed a HC based fracture model for the bulk material that took into account the variability in grain-level properties [12].

Note that an important distinction between the wire-DED Ti–6Al–4V material studied in Refs. [11,12] and the L-PBF Ti–6Al–4V, which is studied here, is that they have drastically different processing conditions. The wire-DED process, also referred to as shape metal deposition, utilizes tungsten inert gas (TIG) welding technology [36], while the L-PBF process utilizes a laser heat source with a spot size on the order of 70–140 μm in diameter. This among other process variations, results in drastically different microstructures wherein the prior-β grains in the wire-DED method are orders of magnitude larger than those in L-PBF Ti–6Al–4V (on the order of 100 μm tall by 90 μm wide [13]). Additionally, the significant differences in the failure behavior between conventionally processed and wire-DED Ti–6Al–4V highlight the importance of explicitly measuring and modeling the fracture behavior of L-PBF Ti–6Al–4V, whose microstructure differs from those in these two other conditions, to design against failure in this material.

As demonstrated in conventionally processed ductile metals, ductile failure behavior depends on stress state; thus, engineers should not rely on data from a single stresss state (e.g., UT) for predicting fracture of components. It is therefore critical to characterize materials under a range of stress states and to develop and calibrate models that capture stress state-dependent failure behavior to ensure the safety of structural components. This is particularly critical for the adoption of AM, where the design freedom that allows for complex geometries and custom components is a hallmark of the technology. To demonstrate the importance of understanding and describing the stress state-dependence of fracture in L-PBF Ti–6Al–4V, the present study evaluates the fracture behavior of this material under a range of stress states, and compares the ability of several fracture models, with varying complexity, to capture this behavior. This work highlights the importance of considering the effects of both stress triaxiality and Lode angle parameter in fracture models, and provides insight on models that best capture this material's fracture behavior.

## 2. Experimental methods

All Ti–6Al–4V samples (~90 wt% Ti, 6 wt% Al, and 4 wt% V in accordance with ASTM F2924 [37]) were manufactured on an EOS M280 L-PBF system using the EOS standard processing parameters for Ti–6Al–4V with a 60 μm layer height, such that the volumetric heat input was 32.4 J/mm$^3$. For all samples, blocks or walls were fabricated using the L-PBF process, then the entire build plate was subjected to a post-processing stress relief heat treatment of 650 °C for 3 h in an argon environment. The samples were then removed from the build plate by wire electrical discharge machining (EDM) for final machining. Samples for the evaluation of fracture behavior of additively manufactured Ti–6Al–4V in this work were machined from the same L-PBF build as those used in the development of the plasticity model for this material [13], with the exception of the equibiaxial tension (EBT) punch samples that were manufactured separately. The microstructure of the Ti–6Al–4V material used in the current study was evaluated previously and is presented in Ref. [13].

Six different sample geometries were machined, from the additively manufactured walls, and used to evaluate the fracture behavior in seven different stress states and in two primary orientations: one in which the properties parallel to the vertical build direction (BD) were probed and one in which the properties perpendicular to the vertical build direction (⊥BD) were probed. The equibiaxial tension punch samples, as detailed in Ref. [38], were machined from the plane orthogonal to the other samples.

Butterfly specimens with geometry optimized by Dunand and Mohr [39], as shown in Fig. 1, were used to evaluate pure shear and combined tension/shear loading under plane stress. Wire EDM was used to machine the outer profile of the butterfly samples and CNC milling was used to machine the reduced thickness gauge region of these samples. Central hole tension (CH) and notched tension (NT) samples, also designed to maintain a plane stress state at fracture with the geometries as shown in Fig. 2, were machined using wire EDM. The central hole tension sample is designed such that it maintains a uniaxial tension stress state up to fracture at the perimeter of the circle in the center of the gauge region. The stress states in the notched tension samples have a smaller Lode angle parameter and slightly larger stress triaxiality, which increases with decreasing notch radii, than uniaxial tension, at the center of the gauge region. The equibiaxial tension punch samples have the highest stress triaxiality of all sample types studied and are the only samples with a negative Lode angle parameter. The set of test samples used was chosen to probe the failure behavior of L-PBF Ti–6Al–4V over a wide range of stress states, as well as to evaluate the ability of multiple fracture models to capture the resulting fracture behavior.

The relationship between the two stress state parameters, $\eta$ and $\bar{\theta}$, under plane stress, as well as the stress state of each sample type probed in this study at fracture are shown in Fig. 3. It is noted that computational modeling of the experiments indicated that the notched tension samples were not under perfect plane stress for the duration of the

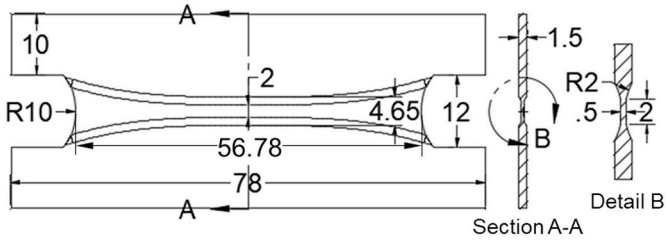


**Fig. 1.** Schematic of the butterfly sample used for pure shear and combined loading stress states (dimensions in mm). Geometry from Ref. [39].

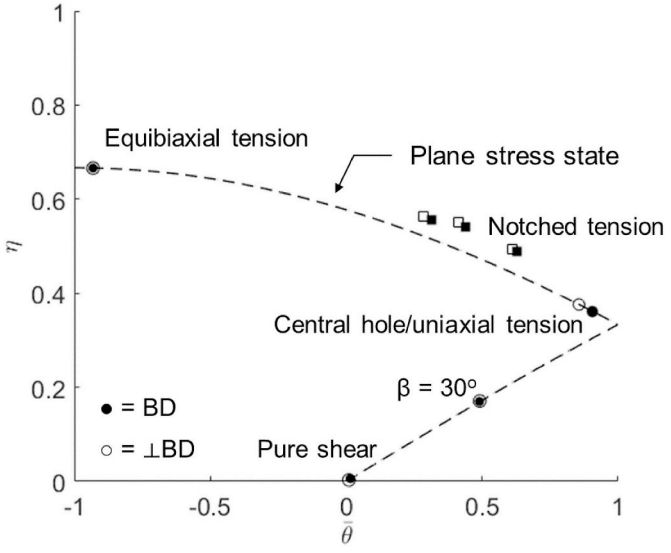


**Fig. 3.** Stress triaxiality versus Lode angle parameter for the condition of plane stress (dashed curve) along with stress state locations of all samples tested (symbols). Square data points represent samples that did not perfectly meet the plane stress condition (as shown by their distance from the ideal plane stress dashed line).

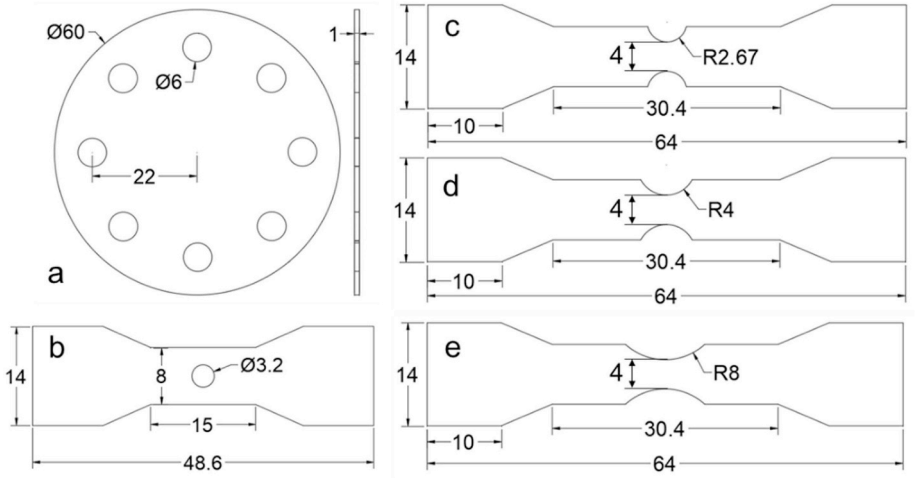


**Fig. 2.** Schematics of the flat fracture specimens tested. (a) Equibiaxial tension punch, (b) 1.5 mm thick central hole, and 1.5 mm thick notched tension specimens with cutout radii of (c) 2.67 mm, (d) 4 mm, and (e) 8 mm. All dimensions in mm.

experiments, but were very close.

Mechanical tests of the butterfly samples were performed using a custom-built dual-actuator hydraulic loading machine (MTS, Inc.) schematically shown in Ref. [13]. The load frame is equipped with two 100 kN load cells to measure force in the vertical direction and one 50 kN load cell to measure force in the horizontal direction. Pure shear tests were completed for two samples in each orientation by loading each sample under displacement control at 0.4 mm/min in the horizontal direction, with the vertical actuator kept at zero force throughout the test. For the combined tension/shear loading tests, both actuators were run under force control, and the angle β can be used to describe the ratio of vertical to horizontal forces during a test as:

$$\beta = \tan^{-1}\left(\frac{\dot{F}_V}{\dot{F}_H}\right) \tag{4}$$

Two butterfly samples in each orientation were subjected to β = 30° loading, with a horizontal loading rate, $\dot{F}_H$, of 0.75 kN/min and a vertical loading rate, $\dot{F}_V$ , of 0.433 kN/min.

Three tests in each orientation were performed on central hole samples and each of the notched tension geometries using an electromechanical load frame (MTS Criterion 43) with a 10 kN load cell. These tests were performed under displacement control loading with an applied strain rate on the order of $10^{-4}$ $s^{-1}$. The equibiaxial tension, or punch tests, were performed on three samples. These were tested using a punch fixture consisting of a 25.4 mm diameter die and a 12.7 mm diameter hemispherical punch, modeled after the fixture in Ref. [38], using an electromechanical load frame (Instron model 4206) with a 150 kN load cell and a punch loading rate of 0.4 mm/min. Teflon sheets were used between the sample and the punch to minimize the effect of friction during loading.

Surface deformation fields were measured using digital image correlation (DIC), a non-contact deformation measurement technique. Three-dimensional DIC (3D DIC) was used for equibiaxial punch tests, while two-dimensional DIC (2D DIC) was used for all other tests. The gauge regions of all samples were painted with a flat white basecoat with a black random speckle pattern on top of the basecoat. Images of the samples were taken at a rate of 1 Hz using one camera for 2D DIC and two cameras for 3D DIC (Point Grey GRAS-50S5M − C) with data capture software (VicSnap, Correlated Solutions) until fracture. For the 3D DIC a calibration target with a 9 x 9 dot pattern and 2.5 mm spacing was used to calibrate the relative positions of the cameras with respect to each other. Vic2D and Vic3D software (Correlated Solutions) were used to compute strains from the images acquired during tests. The image analysis parameters for 2D DIC were set as a subset size of 21 pixels and a step size of 5 pixels, while for the 3D DIC the subset size was 29 pixels and the step size was 7 pixels. Displacement for each 2D DIC test was measured using a virtual vertical extensometer centered in the gauge region with a length of 10 mm for the central hole test, 18 mm for the notched tension samples, and 8 mm for the butterfly samples. Displacement for the punch test samples was calculated comparing the relative displacement of the pixel at the center of the sample, directly above the apex of the punch, and a pixel 11 mm away from the apex, close to the edge of the die. Force data for each test were directly exported from the respective load frames during testing.

Testing was performed up to failure for all samples. Experimentally, failure was defined as separation of the material in the gauge region for central hole and notched tension tests, or the appearance of a visible crack on the sample surface in the digital images for the butterfly and punch tests. Failure in the simulations was defined at the same time (or displacement) where the aforementioned experimental definitions of failure occurred. Using these definitions of failure, the average equivalent strain at fracture among tests in one condition, as well as the average stress triaxiality and average Lode angle parameter throughout the deformation to failure, were all computed using finite element analysis as described in Section 3, and are given in Table 1. These values were used in the calibration of the fracture models described in Section 4.

**Table 1**
Average values of the strain to failure, stress triaxiality, and Lode angle parameter for each test performed.

| Sample Type | Orientation | $\bar{\varepsilon}_f$ | η | $\bar{\theta}$ |
|---|---|---|---|---|
| Pure Shear | BD | 0.091 | 0.006 | 0.016 |
| | ⊥BD | 0.062 | 0.003 | 0.010 |
| β30 | BD | 0.115 | 0.170 | 0.490 |
| | ⊥BD | 0.109 | 0.171 | 0.491 |
| CH | BD | 0.324 | 0.361 | 0.905 |
| | ⊥BD | 0.230 | 0.376 | 0.856 |
| R8 | BD | 0.164 | 0.489 | 0.626 |
| | ⊥BD | 0.148 | 0.494 | 0.611 |
| R4 | BD | 0.125 | 0.540 | 0.440 |
| | ⊥BD | 0.135 | 0.550 | 0.413 |
| R2.67 | BD | 0.112 | 0.555 | 0.315 |
| | ⊥BD | 0.110 | 0.564 | 0.285 |
| Punch | – | 0.120 | 0.667 | −0.931 |

## 3. Finite element simulations

The previously developed, orientation dependent plasticity model was implemented in the finite element analysis (FEA) commercial software ABAQUS [40] and used for simulations of all fracture experiments in the present study. FEA simulations were used to determine the equivalent plastic strain and stress state history at the location of fracture for each sample type.

Simulations of the butterfly samples under pure shear and β = 30° were performed using a FEA model with half the thickness of the experimental geometry, taking advantage of sample symmetry to reduce computational time. The grip regions were modeled as rigid bodies, while the gauge region and transition region between the grips and the gauge region were modeled using the elasto-plastic model of L-PBF Ti–6Al–4V presented in Ref. [13]. The half butterfly geometry was discretized with 126,176 C3D8 elements. For both stress states, two reference nodes were defined for the bottom and top rigid grip sections. For the pure shear condition, a horizontal displacement of 0.6 mm was applied to the top reference node, and all remaining degrees of freedom were fixed for the top and bottom grips. In the simulations of the β = 30° test, force boundary conditions were applied to the top grip reference node in the vertical and horizontal directions at a ratio to meet the β = 30° condition, and all other degrees of freedom for the top and bottom grips were fixed. The simulated displacements for both stress states were extracted from the equivalent top and bottom locations of the 8 mm tall experimental virtual extensometer at the center of the gauge region.

Simulations of the central hole and notched tension tests were performed using a 1/8th model geometry with symmetry boundary conditions applied on the three cut planes of the samples. The model geometries were discretized with the following number of C3D8 elements: 5,824 in the central hole geometry, 1,176 in the R = 2.67 mm NT geometry, 1,232 in the R = 4 mm NT geometry, and 1,456 in the R = 8 mm NT geometry. A 1 mm vertical displacement was applied to a reference node that dictated the vertical displacement of all nodes in the grip region of each sample. Displacement was calculated from nodes at equivalent locations to those of the experimental virtual extensometers.

For all 2D DIC samples, failure was assumed to occur in the center of the gauge region, except for the CH geometry in which failure was assumed to occur at the leftmost or rightmost point on the perimeter of the hole. These locations are where time histories of stress triaxiality, Lode angle parameter, and equivalent plastic strain were extracted for each simulation.

For the punch simulation, the full sample thickness was modeled,

along with ¼ of the circle, and this geometry was discretized with 121,440 C3D8 elements. Symmetry boundary conditions along the two cut planes were applied to the ¼ geometry. In addition to the sample, the punch and clamping fixture were modeled as rigid bodies with frictionless contact between these entities and the sample. This is consistent with the approximation made in Ref. [38] for similar tests, and is justified due to the use of Teflon in the experiments. All degrees of freedom were constrained for nodes along the circumference of the punch specimen and the die/clamping fixture. A 1 mm vertical displacement was applied to the rigid punch during the simulation, while all other degrees of freedom of the punch were constrained. The punch displacement was calculated as the relative displacement between the apex node on the top surface of the specimen and a node 11 mm away from the apex (toward the die edge) on the top surface. The stress triaxiality, Lode angle parameter, and equivalent strain histories were extracted from the apex of the punch specimen, where failure was assumed to initiate.

The plasticity model proposed for L-PBF Ti–6Al–4V in Ref. [13] incorporates a conservative flow curve, which was the lowest stress-strain curve measured in each direction for this material. For the current study, in order to accurately capture the deformation behavior of all fracture tests performed, the flow stress in the plasticity model was taken to be that of the average material behavior in each orientation, implemented as a 4% increase in flow stress over that adopted in Ref. [13]. Comparisons of the simulated and experimentally measured force vs. displacement behavior for each of the samples tested are given in Fig. 4. The model predicts well the elastic and plastic behavior of the material for each geometry, with the maximum error being an over-prediction of the maximum force by 2% in the build direction notched tension R = 2.67 mm sample.

## 4. Calibration of fracture models

In this study, six different ductile fracture models, dependent on neither, one, or both of the stress state parameters of stress triaxiality and Lode angle parameter, were compared to determine their suitability for describing the multiaxial fracture behavior of L-PBF Ti–6Al–4V. While the stress state parameters evolve over the course of elasto-plastic deformation, as shown in Fig. 5, for the description of a fracture condition, an average definition of stress state is needed. Thus, as monotonic loading is used in all tests presented, the average stress triaxiality is approximated as:

$$\eta_{av} = \frac{1}{\bar{\varepsilon}_f}\int_0^{\bar{\varepsilon}_f} \eta \, d\bar{\varepsilon} \tag{5}$$

and the average Lode angle parameter is approximated as:

$$\bar{\theta}_{av} = \frac{1}{\bar{\varepsilon}_f}\int_0^{\bar{\varepsilon}_f} \bar{\theta} \, d\bar{\varepsilon} \tag{6}$$

Four of the models described here consider the equivalent strain to

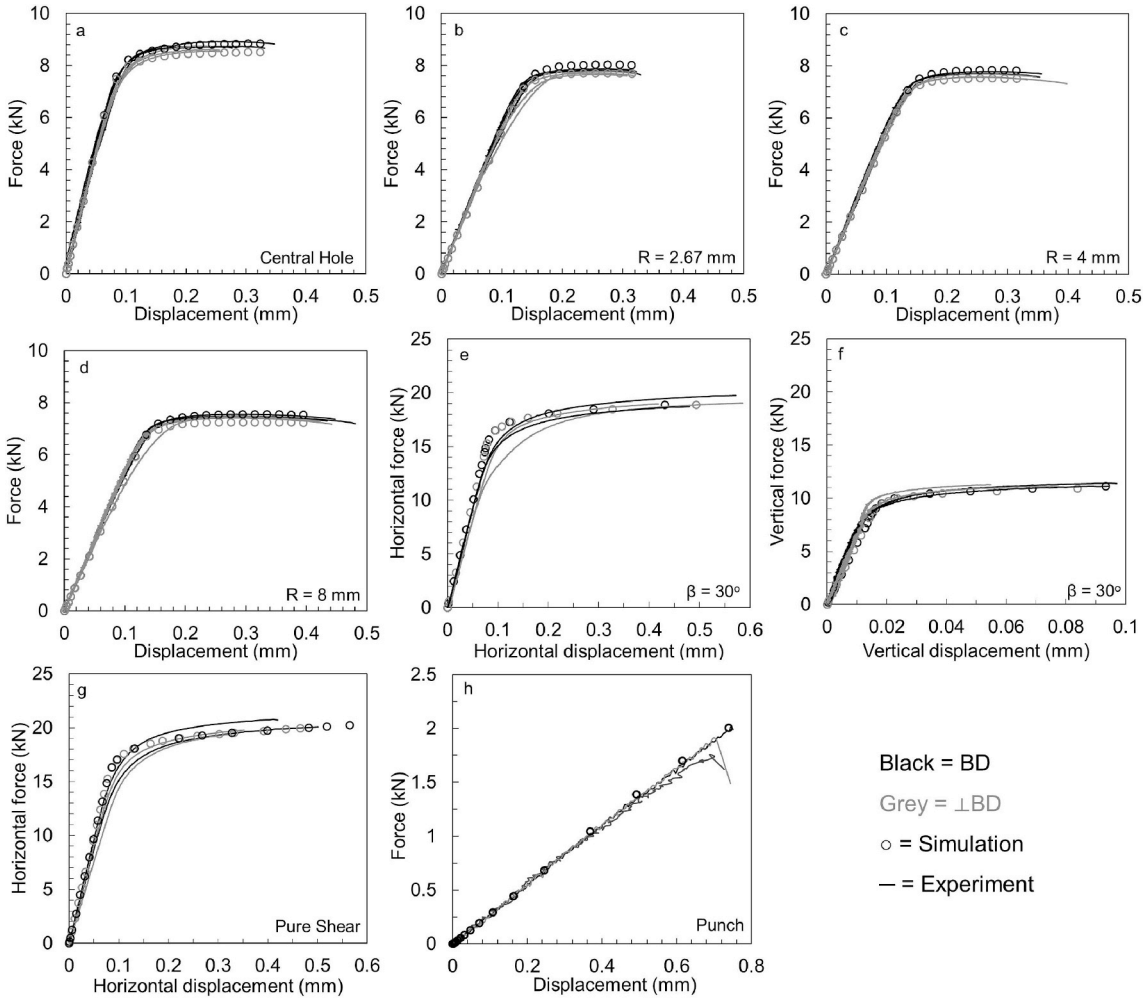


**Fig. 4.** Comparison of experimentally measured and simulated force vs. displacement results for the (a) central hole tension; (b) R = 2.67 mm, (c) R = 4 mm, and (d) R = 8 mm notched tension tests; (e, f) β = 30° combined loading; (g) pure shear loading; and (h) equibiaxial tension punch tests.

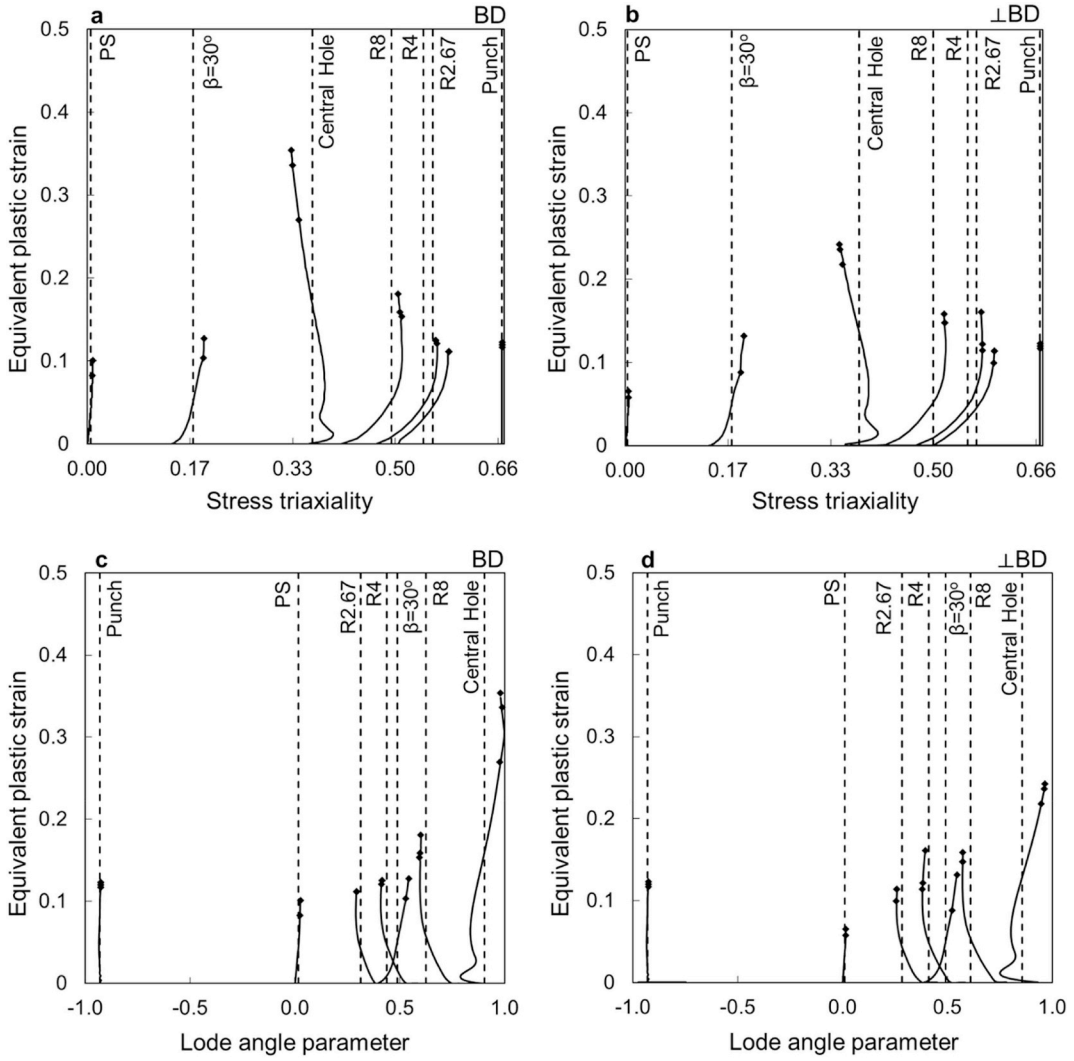


**Fig. 5.** Evolution of the (a, b) stress triaxiality and (c, d) Lode angle parameter (solid lines) up to failure (symbols) for each sample geometry in both the BD (a, c) and ⊥BD (b, d) with the average value of each stress state parameter used in fracture model calibration represented by a vertical dashed line.

failure only as a function of the average stress triaxiality, while two of the models consider the strain to failure as a function of both the average stress triaxiality and Lode angle parameter.

### 4.1. Constant equivalent strain to fracture criterion

The simplest criteria to define the failure of ductile metals is the constant equivalent strain to fracture criterion, which states that fracture occurs in a material when

$$\bar{\varepsilon} = \bar{\varepsilon}_f \tag{7}$$

where $\bar{\varepsilon}_f$ is the critical strain to failure under a given stress state used to define failure (here taken to be uniaxial tension), and $\bar{\varepsilon}$ is the is the equivalent plastic strain in any stress state of interest. For the L-PBF Ti–6Al–4V material, the Hill 1948 description of the equivalent plastic strain under plane stress was used, which is given as [14,28]:

$$d\bar{\varepsilon}^p = \left\{\frac{1}{p}\left[(F+H)(d\varepsilon_{11}^p)^2 + (H+G)(d\varepsilon_{22}^p)^2 + 2H(d\varepsilon_{11}^p)(d\varepsilon_{22}^p)\right] + \frac{1}{2N}(2d\varepsilon_{12}^p)^2\right\}^{0.5} \tag{8}$$

where F, G, H, and N are constants that describe the material's anisotropy, $P = FG + GH + HF$, $\varepsilon_{11}^p$ and $\varepsilon_{22}^p$ are the normal plastic strains, and $\varepsilon_{12}^p$ is the shear strain. In the present study, the strain to failure under uniaxial tension was obtained using the central hole tension test, which maintains a stress state of nearly uniaxial tension all the way to fracture. The average equivalent strain to failure, $\bar{\varepsilon}_f$, for the central hole tests in each orientation is given in Table 1.

### 4.2. Johnson-Cook fracture criterion

The empirical Johnson-Cook ductile fracture model defines the equivalent strain to failure as monotonic decreasing function of stress triaxiality [20]:

$$\bar{\varepsilon}_f = C_1 + C_2\exp(C_3\eta) \tag{9}$$

where $C_1$, $C_2$, and $C_3$ are calibration constants. This model captures well the experimentally observed decreasing ductility with increasing stress triaxiality in the high stress triaxiality regime. However, it was not designed to capture the fracture behavior under low stress triaxialities. The Johnson-Cook model parameters for both material orientations in the present study were calibrated using nonlinear least-squares fitting of the Johnson-Cook equation to the experimental data from the central hole tension test, all three notched tension tests, and the punch tests. The calibrated parameters are given in Table 2.

**Table 2**
Calibrated fracture model parameters for L-PBF Ti–6Al–4V.

| | | | | | | | |
|---|---|---|---|---|---|---|---|
| **Maximum Shear Stress** | Orientation | **C** | **n** | | | | |
| | BD | 42.0 | 0.113 | | | | |
| | ⊥BD | 28.4 | 0.113 | | | | |
| **Johnson-Cook** | Orientation | $\mathbf{C_1}$ | $\mathbf{C_2}$ | $\mathbf{C_3}$ | | | |
| | BD | 0.105 | 16.7 | −12.0 | | | |
| | ⊥BD | 0.111 | 6.94 | −10.8 | | | |
| **Hosford-Coulomb** | Orientation | **a** | **b** | **c** | **n** | | |
| | BD | 1.37 | 0.324 | 0 | 0.042 | | |
| | ⊥BD | 1.44 | 0.230 | 0 | 0.042 | | |
| **Modified Mohr-Coulomb** | Orientation | $\mathbf{c_1}$ | $\mathbf{c_{2\ (MPa)}}$ | $\mathbf{c_\theta^s}$ | $\mathbf{c_\theta^c}$ | **A (MPa)** | **n** |
| | BD | 0 | 651.2 | 0.927 | 1.05 | 1349 | 0.042 |
| | ⊥BD | 0 | 627.2 | 0.933 | 1.05 | 1303 | 0.042 |

### 4.3. Two-branch empirical fit fracture criterion

Another empirical method for constructing a fracture locus for a ductile material in the [η,$\varepsilon_f$] space, as described by Bao et al. [21], is to simply fit the experimental test data, in two distinct stress triaxiality ranges, with polynomials. While this criterion does not incorporate any physics, breaking the plane stress fracture criterion into two regimes does have a physical basis. Namely, Bao et al. hypothesized that in the first, low stress triaxiality range, $0 \le \eta \le 0.33$, fracture occurs due to a combination of shear deformation and void growth, while in the second, high stress triaxiality range, $\eta > 0.33$, fracture is assumed to occur only due to void formation and growth mechanisms. The calibrated empirical curve fit fracture loci for the L-PBF Ti–6Al–4V material are given as:

$$BD,\ \bar{\varepsilon}_f = \begin{cases} 2.67\eta^2 - 0.324\eta + 0.093 & 0 \le \eta \le 0.361 \\ 0.037\eta^{-2.12} & 0.361 < \eta \end{cases} \tag{10}$$

$$\perp BD,\ \bar{\varepsilon}_f = \begin{cases} 0.832\eta^2 - 0.135\eta + 0.062 & 0 \le \eta \le 0.376 \\ 0.059\eta^{-1.37} & 0.376 < \eta \end{cases} \tag{11}$$

The ranges of the low and high stress triaxiality regimes were adjusted for each orientation to capture the central hole test data in the current study. These equations and corresponding fracture locus are only valid for this particular data set for L-PBF Ti–6Al–4V, but the curve fitting does indicate the presence of two distinct regimes of failure for the additively manufactured Ti–6Al–4V material under plane stress.

### 4.4. Maximum shear stress fracture criterion

Plastic deformation occurs by dislocation motion, which is driven by shear stress. Additionally, experimental findings for ductile metals in which localized shear bands and eventual material separation occur at the angle of maximum shear stress/strain (45° from the tensile axis for isotropic materials) can be found in the literature [18]. Based on these observations, the maximum shear failure criterion, which hypothesizes that ductile fracture occurs on the plane of maximum shear stress/strain, defines failure to occur when the maximum shear stress in the stress state of interest is equal to the maximum shear stress at failure under uniaxial tension, and is given as [26]:

$$\tau_{max} = (\tau_{max})_f \tag{12}$$

where

$$\tau_{max} = max\left\{\frac{\sigma_1 - \sigma_2}{2}, \frac{\sigma_2 - \sigma_3}{2}, \frac{\sigma_3 - \sigma_1}{2}\right\} \tag{13}$$

To convert this failure criterion to strain space, a flow rule must be adopted. Approximating the flow behavior under uniaxial tension as a power law relationship between strain and stress as $\sigma = K\varepsilon^n$, the fracture locus in the [η,$\varepsilon_f$] space is given as [26]:

$$\bar{\varepsilon}_f = C\left\{\frac{\sqrt{1+\alpha+\alpha^2}}{2+\alpha}\right\}^{\frac{1}{n}} \quad for\ -\frac{1}{2} < \alpha < 1\ or\ \frac{1}{3} < \eta < \frac{2}{3} \tag{14}$$

$$\bar{\varepsilon}_f = C\left\{\frac{\sqrt{1+\alpha+\alpha^2}}{1-\alpha}\right\}^{\frac{1}{n}} \quad for\ -2 < \alpha < -\frac{1}{2}\ or\ -\frac{1}{3} < \eta < \frac{1}{3} \tag{15}$$

where the relationship between η and α, the strain ratio parameter, is given as

$$\eta = \left(\frac{1}{\sqrt{3}}\right)\left(\frac{(1+\alpha)}{\sqrt{1+\alpha+\alpha^2}}\right) \tag{16}$$

For the L-PBF Ti–6Al–4V material studied here, the strain hardening parameter n = 0.113 was adopted for both build orientations. The calibrated C parameter for each orientation is given in Table 2 for the maximum shear stress fracture criterion.

### 4.5. Modified Mohr-Coulomb fracture criterion

To more accurately define fracture in ductile metals, Bai and Wierzbicki developed the phenomenological modified Mohr-Coulomb fracture model [24], which includes the effects of both stress triaxiality and Lode angle parameter (third invariant of deviatoric stress) in the classical stress-based MC failure criterion [32]. Physically, the MMC fracture criterion takes into account the critical combination of normal stress and shear stress that will cause failure on a given plane in a material. The MMC fracture locus, which is transformed into [$\bar{\varepsilon}_f$, η, $\bar{\theta}$] space as described in detail in Ref. [27], is given as:

$$\bar{\varepsilon}_f[\eta, \bar{\theta}] = \left\{\frac{A}{c_2}\left[c_\theta^s + \frac{\sqrt{3}}{2-\sqrt{3}}(c_\theta^{ax} - c_\theta^s)\left(\sec\left(\frac{\bar{\theta}\pi}{6}\right) - 1\right)\right] \cdot \left[\sqrt{\frac{1+c_1^2}{3}}\cos\left(\frac{\bar{\theta}\pi}{6}\right) + c_1\left(\eta + \frac{1}{3}\sin\left(\frac{\bar{\theta}\pi}{6}\right)\right)\right]\right\}^{-\frac{1}{n}} \tag{17}$$

where

$$c_\theta^{ax} = \begin{cases} 1 & \bar{\theta} \ge 0 \\ c_\theta^c & \bar{\theta} < 0 \end{cases}, \tag{18}$$

$A$ and $n$ are Swift hardening law parameters ($\sigma_y = A(\varepsilon_0 + \bar{\varepsilon}^p)^n$, [11]), and $c_1$, $c_2$, $c_\theta^s$, and $c_\theta^c$ are model parameters, where $c_1$ is referred to as "a friction coefficient", which describes the stress triaxiality dependence and asymmetry of the fracture surface with respect to the Lode angle parameter, $c_2$ influences the magnitude of the failure strains and represents the shear resistance to failure, $c_\theta^s$ controls the Lode angle parameter dependence of the fracture surface, and $c_\theta^c$ controls the asymmetry of the fracture locus with respect to the Lode angle parameter but does not impact the stress triaxiality dependence of the fracture locus [27].

In this study, the MMC model was calibrated using a Matlab

function that finds the minimum of a constrained non-linear multivariable function and determines the model parameters for the best surface fitting of the experimental data points. The calibrated parameters for the MMC fracture model for L-PBF Ti–6Al–4V in two orientations are given in Table 2.

### 4.6. Hosford-Coulomb fracture criterion

The phenomenological Hosford-Coulomb model was developed by Mohr and Marcadet as a fracture initiation model based on the hypothesis that the formation of a primary or secondary band of localization corresponds to the start of fracture in a ductile metal [30]. A motivation for formulating the HC model was that the MC stress-based criterion was found to not fully capture experimental results where localization occurs before void coalescence. To remedy this issue, the HC model takes into account the intermediate principal stress contribution to failure by substituting the Hosford equivalent stress [31] for the maximum shear stress contribution in the MC criterion. The stress-based fracture criterion is then transformed from the principal stress space to equivalent plastic strain space by assuming a von Mises yield surface, non-associated Hill 1948 flow rule, and an isotropic hardening law in Ref. [30]. The Hosford-Coulomb fracture criterion in $[\bar{\varepsilon}_f, \eta, \bar{\theta}]$ space is given as [30]:

$$\bar{\varepsilon}_f[\eta,\bar{\theta}] = b(1+c)^{\frac{1}{n}}\left(\left\{\frac{1}{2}\left((f_1-f_2)^a+(f_2-f_3)^a+(f_1-f_3)^a\right)\right\}^{\frac{1}{a}}+c\left(2\eta+f_1+f_3\right)\right)^{-\frac{1}{n}} \tag{19}$$

where $a$ is the model parameter that controls the dependence on the Lode angle parameter, $b$ controls the overall magnitude of strain to failure and is defined as the average equivalent strain to failure under uniaxial tension in each orientation, and $c$ controls the dependence on the stress triaxiality [11]. The Lode angle parameter is incorporated in the model through the following functions [30]:

$$f_1[\bar{\theta}] = \frac{2}{3}cos\left[\frac{\pi}{6}(1-\bar{\theta})\right];\ f_2[\bar{\theta}] = \frac{2}{3}cos\left[\frac{\pi}{6}(3+\bar{\theta})\right];$$
$$f_3[\bar{\theta}] = \frac{2}{3}cos\left[\frac{\pi}{6}(1+\bar{\theta})\right] \tag{20}$$

The model parameters $a$, $b$, and $c$ for L-PBF Ti–6Al–4V were calibrated through the same methodology as that used to calibrate the MMC parameters as described in Section 4.5.

## 5. Results and discussion

Here, the ability of each of the six failure criteria described above to capture the stress state-dependent fracture behavior of L-PBF Ti–6Al–4V is assessed. The benefits and drawbacks of each model primarily lie in their ability to capture the stress-state dependent fracture behavior with the fewest number of experiments as well as the ease of model calibration. An overarching finding of the study was that similarly to the plasticity behavior, the fracture behavior of L-PBF Ti–6Al–4V was found to be stress state-dependent and anisotropic, which could be captured, at least to some extent, in all but one of the failure criteria studied here.

### 5.1. Comparison of models in 2D space of $\bar{\varepsilon}_f$ versus $\eta$

As noted in Wierzbicki et al. [26], it is difficult to directly compare stress based, strain based, or mixed stress-strain based fracture criteria; however, they can be directly compared for the plane stress condition (Eqn. (3)) for which there is a one-to-one mapping from one space to the other. Therefore, all fracture criteria examined here are plotted in the 2D space of strain to failure as a function of stress triaxiality for the case of plane stress. Only fracture criteria that explicitly incorporate a functional dependence on the Lode angle are plotted in the 3D space of strain to failure as a function of stress triaxiality and Lode angle parameter. For each fracture model considered, it was generally found that a ± 15% margin was needed to capture the experimentally observed variation in strain to failure at a given stress state for L-PBF Ti–6Al–4V. This margin is shown on each of the 2D fracture locus plots.

The constant equivalent strain to failure fracture criterion, which requires a single experiment, assumes that the equivalent strain to failure is the same regardless of stress state. This criterion can vary widely depending on which stress state is used to define the failure equivalent strain. For L-PBF Ti–6Al–4V, if using a uniaxial tension state of stress to define the limit on the equivalent strain to failure, as shown in Fig. 6, the strain to failure in all other stress states is overestimated. This presents two issues: first, this method cannot be used to predict and prevent fracture in stress states other than what it was calibrated based on, as an overestimation of the ductility of a material in engineering design will result in failure; second, if an engineer instead uses a different stress state to define failure strain, providing a lower bound constant strain to fracture criterion, the component may be overdesigned against failure if locations within the component access stress states other than the one used to define failure. Thus, inability of the constant strain to failure fracture criterion to capture the stress state-dependent failure behavior makes this approach inappropriate for the design of components against failure.

The calibrated Johnson-Cook model for L-PBF Ti–6Al–4V captures the equivalent strain to failure behavior for stress triaxialities that are equivalent to uniaxial tension or greater; however, as this model is not intended to predict failure for lower triaxialities, it significantly overestimates the failure behavior under low stress triaxialities as shown in Fig. 7. This model requires tests be performed under at least three stress states for calibration, and model calibration is performed with a simple curve fit to the data. For tension-dominated loading situations, in which void growth mechanisms are assumed to dominate the failure process, the Johnson-Cook model may suffice in describing and predicting fracture behavior.

The two-branch empirical fit fracture criterion is able to capture the data for all seven tests for which it was calibrated, as shown in Fig. 8. However, this is due to the fact that it is composed simply of two empirical fits of the data, and there is no physical meaning incorporated in this model. Therefore, the calibrated equations are only valid for this specific material, and cannot be used to generally describe other material behavior. Given that this fracture criterion is based on simple empirical fits, the model accuracy will increase with the number of tests performed.

The maximum shear stress fracture criterion captures the stress triaxiality dependent failure behavior of the material very well, while only requiring one test condition - pure shear - for calibration. As shown in Fig. 9, this fracture model predicts the equivalent strain to failure conservatively for both build orientations, in all stress states tested, which is preferred to overestimating the ductility. As described above, this model does have physical significance in that it assumes fracture occurs at a critical value of the maximum shear stress present in an arbitrary stress state. However, while this criterion requires only one test, pure shear tests are challenging to carry out due to either limitations in lab equipment (e.g., the access to only uniaxial test frames) or challenges with achieving pure shear loading up to failure [41,42]. Therefore, the experimental measurement of failure strain under pure shear may be assumed to be a lower bound for failure [43].

Figs. 10 and 11 show the 3D MMC and HC models plotted in the 2D stress triaxiality versus strain to failure space for the case of plane stress. The MMC and HC models are very similar to each other and to the empirical curve fit and maximum shear stress criteria in this space. Comparing just the MMC and HC models, the MMC model predicts a higher equivalent strain to failure under perfect plane stress uniaxial tension for both the BD and ⊥BD samples, by 21% or 43% change, respectively.

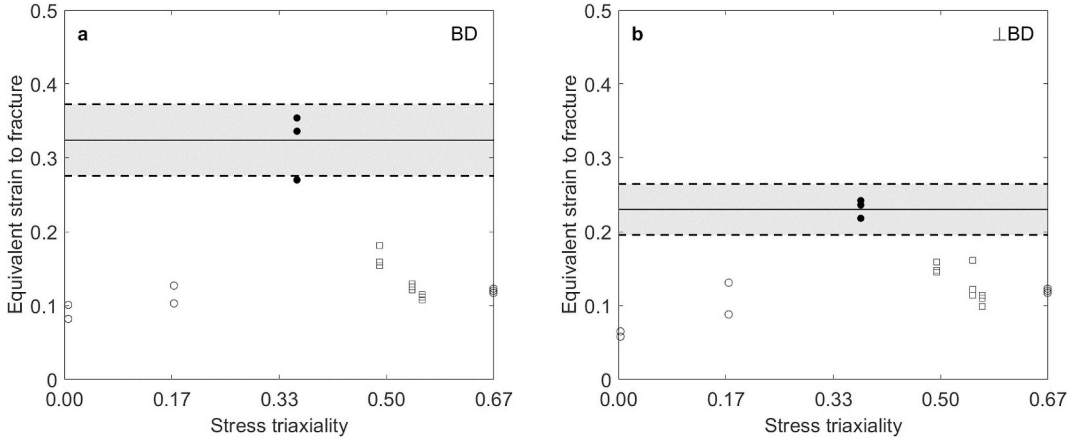


**Fig. 6.** Constant equivalent strain fracture locus (solid black line) for L-PBF Ti–6Al–4V, based only on strain to failure under uniaxial tension (central hole tests) whose tensile axis is in the (a) vertical build direction and (b) perpendicular to the vertical build direction compared to all experimental data (symbols). Shaded area bounded with dashed lines represents ± 15% margin in the average equivalent strain to fracture represented by the solid line. Filled data points were used for calibration of the model.

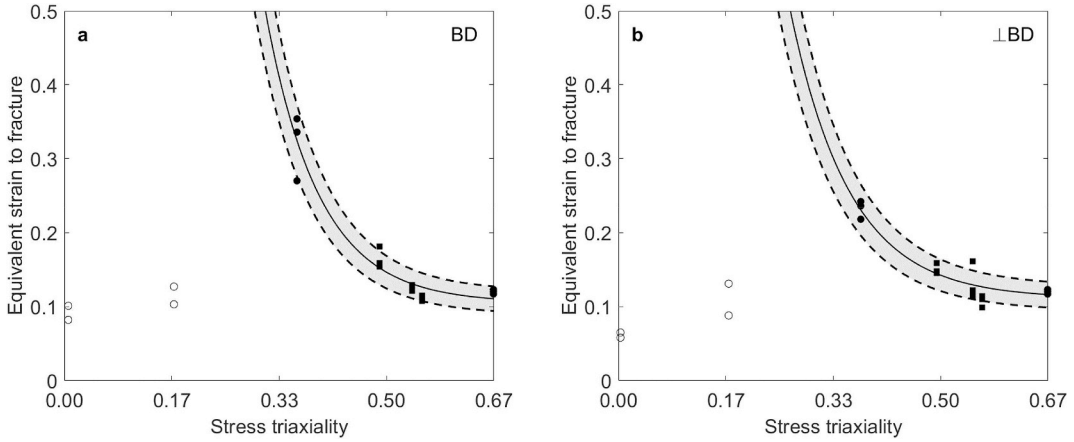


**Fig. 7.** Johnson-Cook fracture locus (solid black line) for L-PBF Ti–6Al–4V whose tensile axis is in the (a) vertical build direction and (b) perpendicular to the vertical build direction compared to all experimental data (symbols). Shaded area bounded with dashed lines represents ± 15% margin in the average equivalent strain to fracture represented by the solid line. Filled data points were used for calibration of the model.

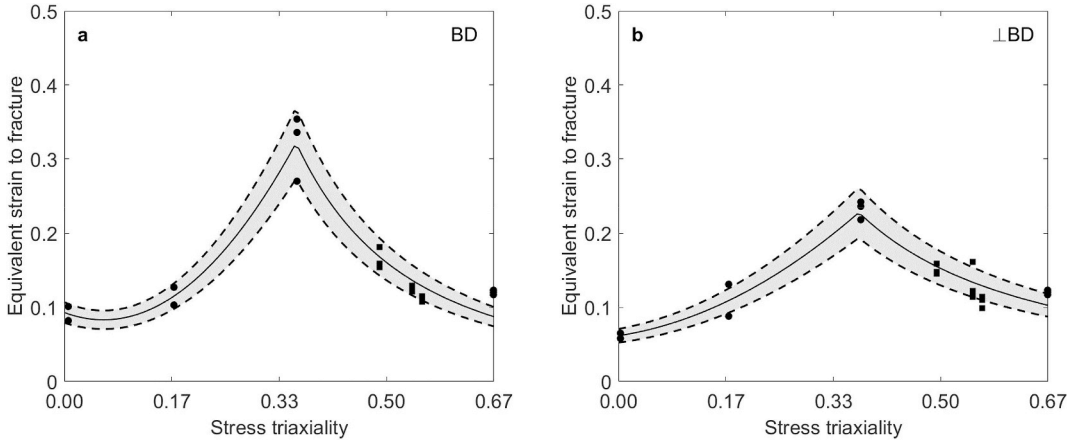


**Fig. 8.** Two-branch empirical fit fracture locus (solid black line) for L-PBF Ti–6Al–4V whose tensile axis is in the (a) vertical build direction and (b) perpendicular to the vertical build direction compared to all experimental data (symbols). Shaded area bounded with dashed lines represents ± 15% margin in the average equivalent strain to fracture represented by the solid line. Filled data points were used for calibration of the model.

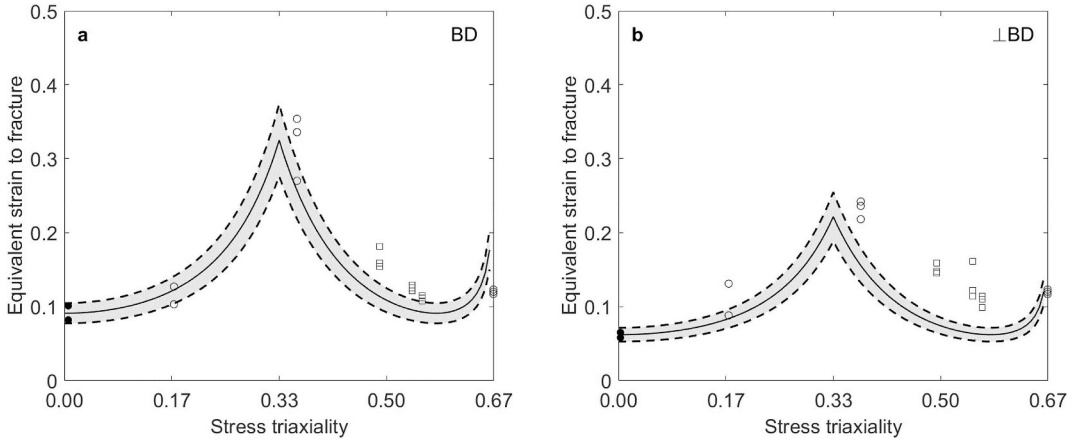


**Fig. 9.** Maximum shear stress criterion fracture locus (solid black line) for L-PBF Ti–6Al–4V whose tensile axis is in the (a) vertical build direction and (b) perpendicular to the vertical build direction compared to all experimental data (symbols). Shaded area bounded with dashed lines represents ± 15% margin in the average equivalent strain to fracture represented by the solid line. Filled data points were used for calibration of the model.

The MMC model, HC model, empirical curve fit criterion, and maximum shear stress criterion all accurately capture the equivalent strain to failure as a function of stress triaxiality, over a wide range of stress triaxiality values, and under plane stress, for L-PBF Ti–6Al–4V. However, for the fracture criterion considered in this study, the influence of the Lode angle parameter is only fully considered using the MMC and HC models.

### 5.2. Comparison of models in 3D space of $\bar{\varepsilon}_f$ versus $\eta$ versus $\bar{\theta}$

Both the MMC and HC fracture criteria explicitly incorporate the effect of Lode angle parameter on failure behavior, which was found to be important in fully understanding the stress state-dependence of the failure behavior of L-PBF Ti–6Al–4V. The 3D fracture surfaces of the MMC and HC models, using the calibrated parameters in Table 2, are shown in Figs. 12 and 13. When plotting these 3D fracture loci on the 2D plane of equivalent strain to failure versus Lode angle parameter, the dependence of fracture strain on Lode angle parameter of the material is made clear, as shown in Figs. 14 and 15.

The MMC fracture criterion for L-PBF Ti–6Al–4V, calibrated using five test geometries, results in $c_1 = 0$ for both material orientations, as shown in Table 2. In this case, the MMC model has, for a given Lode angle, no dependence on stress triaxiality. The parameter $c_\theta^s$, calibrated to be 1.05 and 1.04 for the BD and ⊥BD material, respectively, controls the asymmetry of the fracture locus with respect the Lode angle parameter. This asymmetry allows for the behavior of the negative Lode angle parameter equibiaxial tension samples to be captured by the calibrated fracture surface.

The HC fracture criterion, calibrated using five test geometries, results in a calibrated value of 0 for the parameter $c$ in both material orientations, meaning that, for a constant Lode angle parameter, the calibrated criterion is independent of stress triaxiality, and the fracture locus is symmetric with respect to the Lode angle parameter [30]. The symmetry, with respect to Lode angle parameter, in the HC model captures the experimental equivalent strain data points for all of the positive Lode angle parameter tests well; however, it fails to capture the equibiaxial tension failure. There is an 85% and 57% difference, for the BD and ⊥BD materials, respectively, between the average experimental equibiaxial tension equivalent strain to failure and the fracture surface predicted strain to failure at the same ($\eta$, $\bar{\theta}$) coordinates. One advantage of the calibrated HC model for the L-PBF Ti–6Al–4V material is that it captures stress state-dependent failure, while also more conservatively predicting the failure strain under uniaxial tension, compared to the calibrated MMC model, in both orientations.

However, the clear advantage of the MMC model over the HC model for L-PBF Ti–6Al–4V is the MMC model's ability to capture any asymmetry in Lode angle parameter dependence through its $c_\theta^s$ model parameter. The HC model, with $c = 0$, does not have another parameter

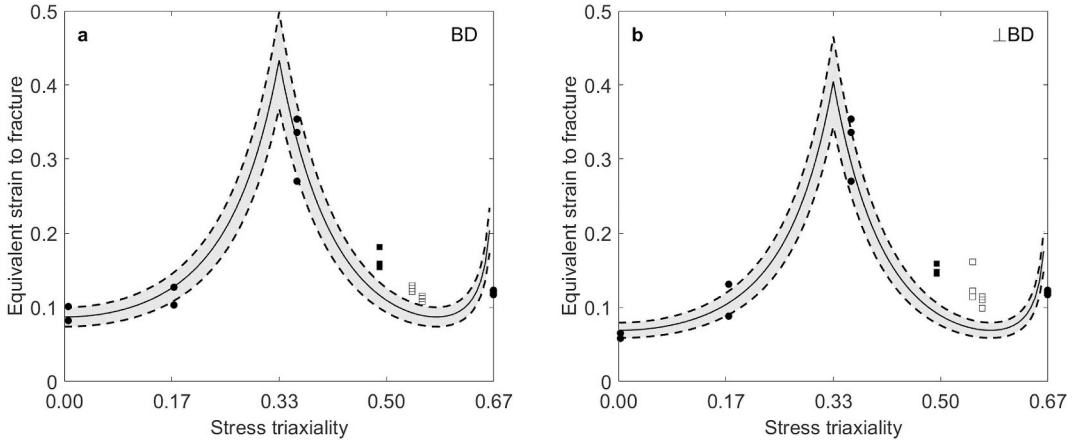


**Fig. 10.** Modified Mohr-Coulomb fracture locus (solid black line) for L-PBF Ti–6Al–4V whose tensile axis is in the (a) vertical build direction and (b) perpendicular to the vertical build direction compared to all experimental data (symbols). Shaded area bounded with dashed lines represents ± 15% margin in the average equivalent strain to fracture represented by the solid line. Filled data points were used for calibration of the model.

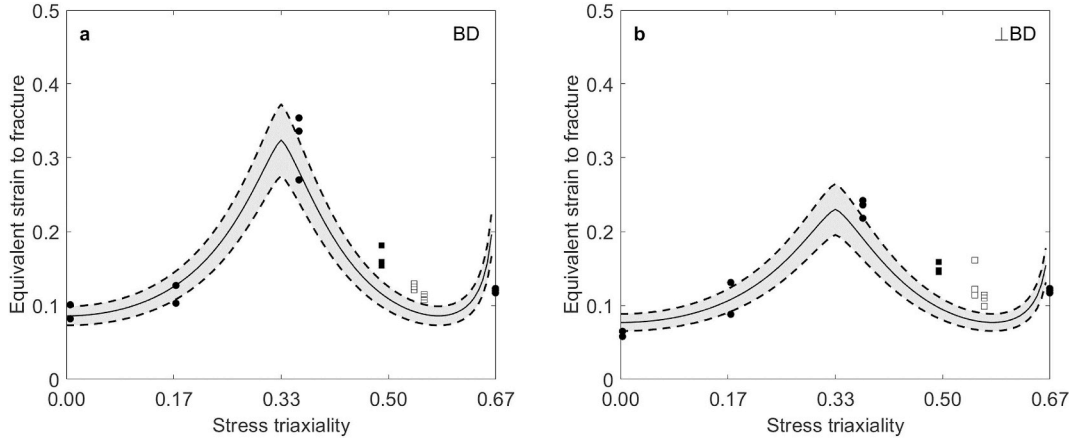


**Fig. 11.** Hosford-Coulomb fracture locus (solid black line) for L-PBF Ti–6Al–4V whose tensile axis is in the (a) vertical build direction and (b) perpendicular to the vertical build direction compared to all experimental data (symbols). Shaded area bounded with dashed lines represents ± 15% margin in the average equivalent strain to fracture represented by the solid line. Filled data points were used for calibration of the model.

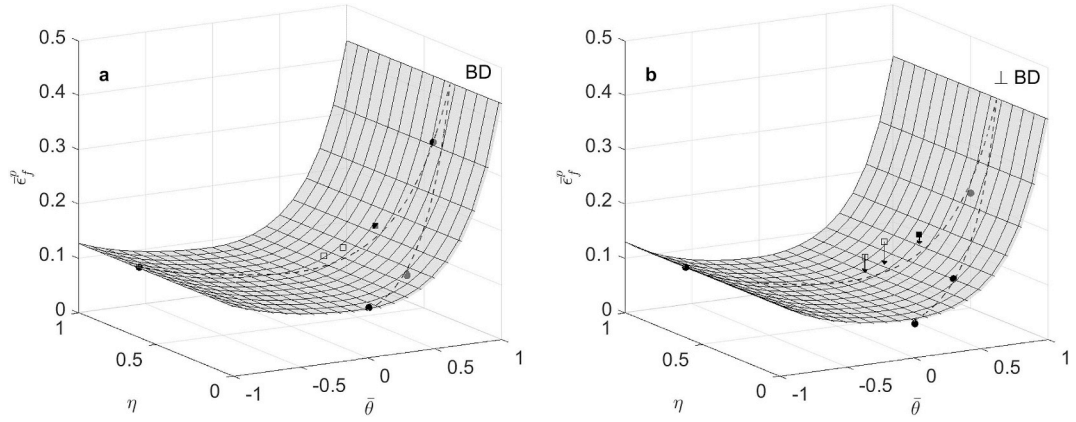


**Fig. 12.** Calibrated three-dimensional MMC fracture locus (surface) for L-PBF Ti–6Al–4V in the (a) build direction and (b) perpendicular build direction compared to all experimental data (symbols). Dashed line on the surface represents the plane stress relationship between the two stress state parameters. Arrows, if present, indicate the distance and direction of the experimental data point to the calibrated fracture surface. Filled data points were used for calibration of the model.

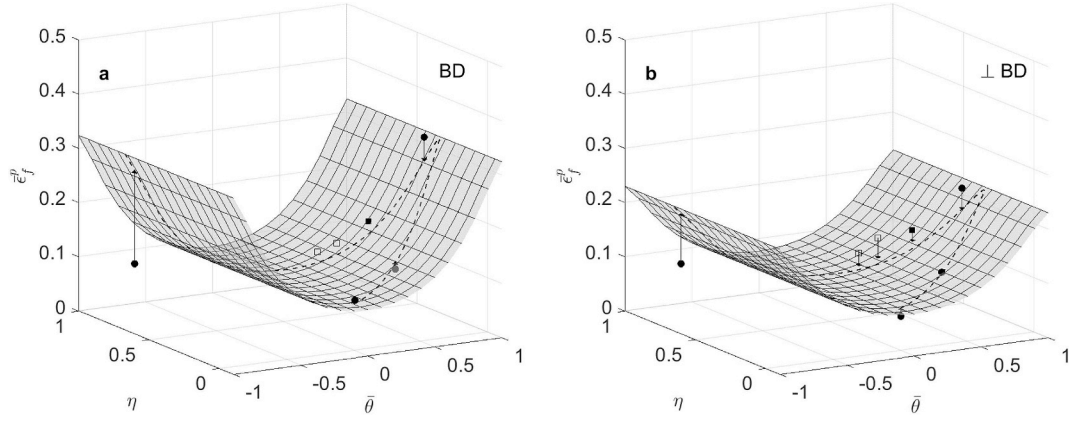


**Fig. 13.** Calibrated three-dimensional HC fracture locus (surface) for L-PBF Ti–6Al–4V in the (a) build direction and (b) perpendicular build direction compared to all experimental data (symbols). Dashed line on the surface represents the plane stress relationship between the two stress state parameters. Arrows, if present, indicate the distance and direction of the experimental data point to the calibrated surface. Filled data points were used for calibration of the model.

to capture asymmetry of equivalent strain to failure with respect to the Lode angle parameter and simultaneously remain independent of the stress triaxiality (for a given Lode angle parameter), as observed in the calibrated MMC model.

The stress state-dependent ductile failure of L-PBF Ti–6Al–4V is best captured with the maximum shear stress and MMC fracture criteria, whereas each of these models has benefits and drawbacks. The primary benefit of the maximum shear stress criterion is that it captures the trend of the equivalent failure strain over a wide range of stress states while only using a single test for calibration. The key drawbacks of the maximum shear stress failure criterion are that it generally underestimates the equivalent failure strain, which could lead to overdesign

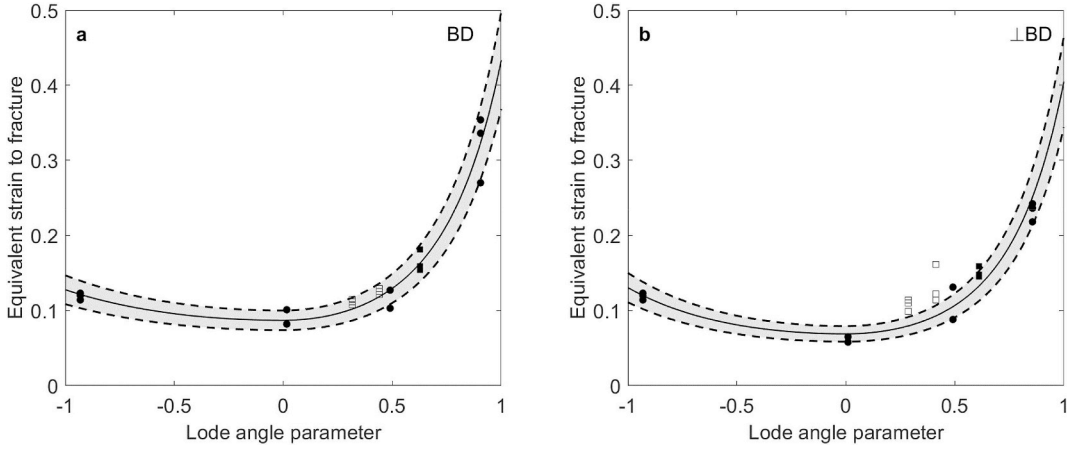


**Fig. 14.** Calibrated MMC fracture locus (solid black line) in the space of Lode angle parameter versus strain to failure, highlighting the importance of Lode angle parameter, for L-PBF Ti–6Al–4V in the (a) build direction and (b) perpendicular build direction compared to all experimental data (symbols). Shaded area bounded with dashed lines represents ± 15% margin in the average equivalent strain to fracture represented by the solid line. Filled data points were used for calibration of the model.

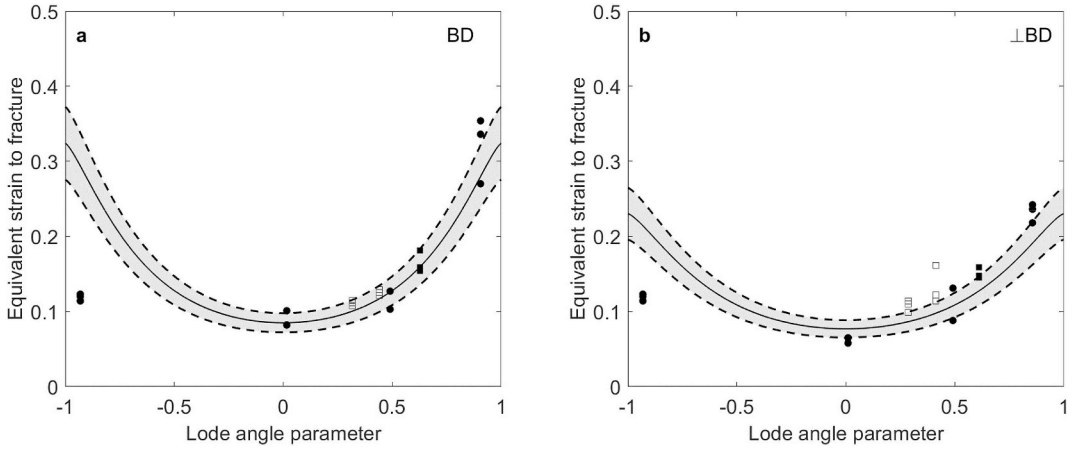


**Fig. 15.** Calibrated HC fracture locus (solid black line) in the space of Lode angle parameter versus strain to failure, highlighting the importance of the Lode angle parameter, for L-PBF Ti–6Al–4V in the (a) build direction and (b) perpendicular build direction compared to all experimental data (symbols). Shaded area bounded with dashed lines represents ± 15% margin in the average equivalent strain to fracture represented by the solid line. Filled data points were used for calibration of the model.

of components, and that achieving the pure shear stress state in an experimental setting can be difficult. The primary benefits of the MMC fracture criterion are that it explicitly incorporates a dependence on both $\eta$ and $\bar{\theta}$ and it is able to capture the asymmetry of the failure behavior with respect to Lode angle parameter that was observed in the L-PBF Ti–6Al–4V material. A drawback of the MMC model is the number of tests required to accurately calibrate the model over a range of stress states.

## 6. Conclusions

For the first time, the fracture behavior of L-PBF Ti–6Al–4V was measured over a wide range of stress states in two build orientations, and a range of ductile failure models were calibrated and compared. Using a combined experimental and computational approach, the equivalent strain to failure, as a function of stress state parameters stress triaxiality and Lode angle parameter, was calculated for seven different stress states. Six different failure criteria were compared and the primary conclusions are:

- The ductile failure of L-PBF Ti–6Al–4V was found to depend significantly on stress state, where both stress triaxiality and Lode angle parameter are needed to fully define the stress state and its influence on failure strain. This highlights the importance of understanding fracture properties of additively manufactured materials under a range of stress states in order to prevent failure of structural components designed with the freedom of AM.
- The MMC model, calibrated with five tests and able to capture the asymmetry of the equivalent strain to failure with respect to the Lode angle parameter, was found to be most appropriate for capturing and predicting the effects of both of the stress state parameters on fracture.
- The maximum shear stress fracture criterion, which was calibrated with only one test, albeit one that can be challenging to conduct experimentally, captured conservatively the trend of equivalent strain to failure with respect to the stress triaxiality.
- The equivalent strain to failure for all stress states was higher for BD samples compared to ⊥BD samples, which every model evaluated was able to capture.
- A margin of ± 15% surrounding the two-branch empirical fit, maximum shear stress, MMC, and HC fracture criterions was appropriate for describing the experimental variation of the equivalent strain to failure in L-PBF Ti–6Al–4V.

## Acknowledgments

The financial support provided by the National Science Foundation through award numbers CMMI-1402978 and CMMI-1652575 is gratefully acknowledged. Any opinions, findings, and conclusions or recommendations expressed in this material are those of the authors and do not necessarily reflect the views of the National Science Foundation. The samples were fabricated at Penn State's Center for Innovative Materials Processing through Direct Digital Deposition (CIMP-3D).

## Data availability

All relevant data are available from the authors.

## Appendix A. Supplementary data

Supplementary data to this article can be found online at https://doi.org/10.1016/j.msea.2019.05.097.

## References

[1] T. DebRoy, H.L. Wei, J.S. Zuback, T. Mukherjee, J.W. Elmer, Milewski JO, A.M. Beese, A. Wilson-Heid, A. De, W. Zhang, Additive manufacturing of metallic components – process, structure and properties, Prog. Mater. Sci. 92 (2018) 112–224, https://doi.org/10.1016/j.pmatsci.2017.10.001.

[2] D.D. Gu, W. Meiners, K. Wissenbach, R. Poprawe, Laser additive manufacturing of metallic components: materials, processes and mechanisms, Int. Mater. Rev. 57 (2012) 133–164, https://doi.org/10.1179/1743280411Y.0000000014.

[3] M. Brandt, S.J. Sun, M. Leary, S. Feih, J. Elambasseril, Q.C. Liu, High-value SLM aerospace components: from design to manufacture, Adv. Mater. Res. 633 (2013) 135–147 https://doi.org/10.4028/www.scientific.net/AMR.633.135.

[4] L.E. Murr, S.A. Quinones, S.M. Gaytan, M.I. Lopez, A. Rodela, E.Y. Martinez, D.H. Hernandez, E. Martinez, F. Medina, R.B. Wicker, Microstructure and mechanical behavior of Ti-6Al-4V produced by rapid-layer manufacturing, for biomedical applications, J. Mech. Behav. Biomed. Mater. 2 (2009) 20–32, https://doi.org/10.1016/j.jmbbm.2008.05.004.

[5] G. Lütjering, J.C. Williams, Titanium : Engineering Materials and Processes, Second, (2007).

[6] H. Gong, K. Rafi, H. Gu, G.D. Janaki Ram, T. Starr, B. Stucker, Influence of defects on mechanical properties of Ti-6Al-4V components produced by selective laser melting and electron beam melting, Mater. Des. 86 (2015) 545–554, https://doi.org/10.1016/j.matdes.2015.07.147.

[7] P. Kumar, O. Prakash, U. Ramamurty, Micro-and meso-structures and their influence on mechanical properties of selectively laser melted Ti-6Al-4V, Acta Mater. 154 (2018) 246–260, https://doi.org/10.1016/j.actamat.2018.05.044.

[8] A.E. Wilson-Heid, Z. Wang, B. McCornac, A.M. Beese, Quantitative relationship between anisotropic strain to failure and grain morphology in additively manufactured Ti-6Al-4V, Mater. Sci. Eng. A 706 (2017) 287–294, https://doi.org/10.1016/j.msea.2017.09.017.

[9] D. Greitemeier, F. Palm, F. Syassen, T. Melz, Fatigue performance of additive manufactured TiAl6V4 using electron and laser beam melting, Int. J. Fatigue (2016), https://doi.org/10.1016/j.ijfatigue.2016.05.001.

[10] P. Edwards, M. Ramulu, Fatigue performance evaluation of selective laser melted Ti–6Al–4V, Mater. Sci. Eng. A 598 (2014) 327–337, https://doi.org/10.1016/j.msea.2014.01.041.

[11] T. Tancogne-Dejean, C.C. Roth, U. Woy, D. Mohr, Probabilistic fracture of Ti-6Al-4V made through additive layer manufacturing, Int. J. Plast. 78 (2016) 145–172, https://doi.org/10.1016/j.ijplas.2015.09.007.

[12] M.B. Gorji, T. Tancogne-Dejean, D. Mohr, Heterogeneous random medium plasticity and fracture model of additively-manufactured Ti-6Al-4V, Acta Mater. 148 (2018) 442–455, https://doi.org/10.1016/j.actamat.2018.02.025.

[13] A.E. Wilson-Heid, S. Qin, A.M. Beese, Anisotropic multiaxial plasticity model for laser powder bed fusion additively manufactured Ti-6Al-4V, Mater. Sci. Eng. A 738 (2018) 90–97, https://doi.org/10.1016/j.msea.2018.09.077.

[14] R. Hill, A theory of the yielding and plastic flow of anisotropic metals, Proc R Soc A Math Phys Eng Sci 193 (1948) 281–297, https://doi.org/10.1098/rspa.1948.0045.

[15] F.A. McClintock, A criterion for ductile fracture by the growth of holes, J. Appl. Mech. 35 (1968) 363–371.

[16] A.L. Gurson, Continuum theory of ductile rupture by void nucleation and growth: Part I—yield criteria and flow rules for porous ductile media, J. Eng. Mater. Technol. 99 (1977) 2, https://doi.org/10.1115/1.3443401.

[17] J.R. Rice, D.M. Tracey, On the ductile enlargement of voids in triaxial stress fields, J. Mech. Phys. Solids 17 (1969) 201–217, https://doi.org/10.1016/0022-5096(69)90033-7.

[18] V. Tvergaard, A. Needleman, Analysis of the cup-cone fracture in a round tensile bar, Acta Metall. 32 (1984) 157–169, https://doi.org/10.1016/0001-6160(84)90213-X.

[19] K. Nahshon, J.W. Hutchinson, Modification of the gurson model for shear failure, Eur. J. Mech. A Solid. 27 (2008) 1–17, https://doi.org/10.1016/j.euromechsol.2007.08.002.

[20] G.R. Johnson, W.H. Cook, Fracture characteristics of three metals subjected to various strains, strain rates, temperatures and pressures, Eng. Fract. Mech. 21 (1985) 31–48 https://doi.org/10.1016/0013-7944(85)90052-9.

[21] Y. Bao, T. Wierzbicki, On fracture locus in the equivalent strain and stress triaxiality space, Int. J. Mech. Sci. 46 (2004) 81–98, https://doi.org/10.1016/j.ijmecsci.2004.02.006.

[22] M.S. Mirza, D.C. Barton, P. Church, The effect of stress triaxiality and strain-rate on the fracture characteristics of ductile metals, J. Mater. Sci. 31 (1996) 453–461, https://doi.org/10.1007/BF01139164.

[23] T. Coppola, L. Cortese, P. Folgarait, The effect of stress invariants on ductile fracture limit in steels, Eng. Fract. Mech. 76 (2009) 1288–1302, https://doi.org/10.1016/j.engfracmech.2009.02.006.

[24] Y. Bai, T. Wierzbicki, A new model of metal plasticity and fracture with pressure and Lode dependence, Int. J. Plast. 24 (2008) 1071–1096, https://doi.org/10.1016/j.ijplas.2007.09.004.

[25] M.C. Shaw, A critical review of mechanical failure criteria, J. Eng. Mater. Technol. 106 (1984) 219, https://doi.org/10.1115/1.3225705.

[26] T. Wierzbicki, Y. Bao, Y.W. Lee, Y. Bai, Calibration and evaluation of seven fracture models, Int. J. Mech. Sci. 47 (2005) 719–743, https://doi.org/10.1016/j.ijmecsci.2005.03.003.

[27] Y. Bai, T. Wierzbicki, Application of extended Mohr-Coulomb criterion to ductile fracture, Int. J. Fract. 161 (2010) 1–20, https://doi.org/10.1007/s10704-009-9422-8.

[28] A.M. Beese, M. Luo, Y. Li, Y. Bai, T. Wierzbicki, Partially coupled anisotropic fracture model for aluminum sheets, Eng. Fract. Mech. 77 (2010) 1128–1152, https://doi.org/10.1016/j.engfracmech.2010.02.024.

[29] Y. Lou, H. Huh, Extension of a shear-controlled ductile fracture model considering the stress triaxiality and the Lode parameter, Int. J. Solids Struct. 50 (2013) 447–455, https://doi.org/10.1016/j.ijsolstr.2012.10.007.

[30] D. Mohr, S.J. Marcadet, Micromechanically-motivated phenomenological Hosford-Coulomb model for predicting ductile fracture initiation at low stress triaxialities, Int. J. Solids Struct. 67 (68) (2015) 40–55, https://doi.org/10.1016/j.ijsolstr.2015.02.024.

[31] W.F. Hosford, A generalized isotropic yield criterion, J. Appl. Mech. (1972) 607–609.

[32] J.F. Labuz, A. Zang, Mohr–coulomb failure criterion, Rock Mech. Rock Eng. 45 (2012) 975–979, https://doi.org/10.1007/s00603-012-0281-7.

[33] J. Papasidero, V. Doquet, D. Mohr, Ductile fracture of aluminum 2024-T351 under proportional and non-proportional multi-axial loading: Bao-Wierzbicki results revisited, Int. J. Solids Struct. 69 (70) (2015) 459–474, https://doi.org/10.1016/j.ijsolstr.2015.05.006.

[34] J.T. Hammer, Plastic Deformation and Ductile Fracture of Ti-6Al-4V under Various Loading Conditions, The Ohio State University, 2012.

[35] J.T. Hammer, J.D. Seidt, A. Gilat, Influence of stress state on the ductile fracture of Ti-6Al-4V, Fracture and Fatigue, Volume 7: Proceedings of the 2013 Annual Conference on Experimental and Applied Mechanics, 2014, pp. 85–90.

[36] B. Baufeld, O Van der Biest, R. Gault, Additive manufacturing of Ti-6Al-4V components by shaped metal deposition: microstructure and mechanical properties, Mater. Des. 31 (2010) S106–S111, https://doi.org/10.1016/j.matdes.2009.11.032.

[37] ASTM International, F2924: Standard Specification for Additive Manufacturing Titanium-6 Aluminum-4 Vanadium with Powder Bed Fusion, (2014).

[38] C.C. Roth, D. Mohr, Ductile fracture experiments with locally proportional loading histories, Int. J. Plast. 79 (2016) 328–354, https://doi.org/10.1016/j.ijplas.2015.08.004.

[39] M. Dunand, D. Mohr, Optimized butterfly specimen for the fracture testing of sheet materials under combined normal and shear loading, Eng. Fract. Mech. 78 (2011) 2919–2934, https://doi.org/10.1016/j.engfracmech.2011.08.008.

[40] Simulia, Abaqus User Manual V2016, (2016).

[41] A. Ghahremaninezhad, K. Ravi-Chandar, Ductile failure behavior of polycrystalline Al 6061-T6 under shear dominant loading, Int. J. Fract. 180 (2013) 23–39, https://doi.org/10.1007/s10704-012-9793-0.

[42] S.S. Haltom, S. Kyriakides, K. Ravi-Chandar, Ductile failure under combined shear and tension, Int. J. Solids Struct. 50 (2013) 1507–1522, https://doi.org/10.1016/j.ijsolstr.2012.12.009.

[43] A.J. Gross, K. Ravi-Chandar, On the deformation and failure of Al 6061-T6 at low triaxiality evaluated through in situ microscopy, Int. J. Fract. 200 (2016) 185–208, https://doi.org/10.1007/s10704-016-0078-x.